The Astrophysical Journal, 688:669–682, 2008 November 20

PREDICTING OBSERVATIONAL SIGNATURES OF CORONAL HEATING BY ALFVÉN WAVES AND NANOFLARES

P. Antolin[1] and K. Shibata
Kwasan Observatory, Kyoto University, Yamashina, Kyoto, 607-8471, Japan; antolin@kwasan.kyoto-u.ac.jp, shibata@kwasan.kyoto-u.ac.jp

T. Kudoh and D. Shiota
National Astronomical Observatory of Japan, 2-21-1, Osawa, Mitaka, Tokyo, 181-8588, Japan; kudoh@th.nao.ac.jp, shiota@cfca.jp

and

D. Brooks[2]
Space Science Division, Naval Research Laboratory, Washington, DC 20375; dhbrooks@ssd5.nrl.navy.mil
Received 2008 April 18; accepted 2008 July 17

ABSTRACT

Alfvén waves can dissipate their energy by means of nonlinear mechanisms, and constitute good candidates to heat and maintain the solar corona to the observed few million degrees. Another appealing candidate is nanoflare reconnection heating, in which energy is released through many small magnetic reconnection events. Distinguishing the observational features of each mechanism is an extremely difficult task. On the other hand, observations have shown that energy release processes in the corona follow a power-law distribution in frequency whose index may tell us whether small heating events contribute substantially to the heating or not. In this work we show a link between the power-law index and the operating heating mechanism in a loop. We set up two coronal loop models: in the first model Alfvén waves created by footpoint shuffling nonlinearly convert to longitudinal modes which dissipate their energy through shocks; in the second model numerous heating events with nanoflare-like energies are input randomly along the loop, either distributed uniformly or concentrated at the footpoints. Both models are based on a 1.5-dimensional MHD code. The obtained coronae differ in many aspects; for instance, in the flow patterns along the loop and the simulated intensity profile that *Hinode* XRT would observe. The intensity histograms display power-law distributions whose indexes differ considerably. This number is found to be related to the distribution of the shocks along the loop. We thus test the observational signatures of the power-law index as a diagnostic tool for the above heating mechanisms and the influence of the location of nanoflares.

Subject headings: Sun: corona — Sun: flares — MHD — waves

1. INTRODUCTION

The coronal heating problem, the heating of the solar corona up to a few hundred times the average temperature of the underlying photosphere, is one of the most perplexing and to date unresolved problems in astrophysics. Alfvén waves produced by the constant turbulent convective motions in the subphotospheric region (Alfvén 1947) have been shown to transport enough energy to heat and maintain a corona (Uchida & Kaburaki 1974; Wentzel 1974). This is known as the the Alfvén wave heating model (Hollweg et al. 1982; Kudoh & Shibata 1999). Many dissipating mechanisms for Alfvén waves have been proposed, such as mode conversion, phase mixing, or resonant absorption (see reviews by, e.g., Erdélyi 2004; Erdélyi & Ballai 2007 and further references therein). Another promising coronal heating candidate mechanism is the nanoflare reconnection heating model. The nanoflare reconnection process was first suggested by Parker (1988), who considered a magnetic flux tube as being composed by a myriad of magnetic field lines braided into each other by continuous footpoint shuffling. Many current sheets in the magnetic flux tube would be created randomly along the tube that would lead to many magnetic reconnection events, releasing energy impulsively and sporadically in small quantities of the order of 10^{24} erg or less (nanoflares), uniformly along the tube. The energy flux carried by the slow modes generated in the reconnection events is expected to be 1 order of magnitude higher than the energy flux carried by the generated Alfvén waves (Takeuchi & Shibata 2001). Hence, in this picture the corona would be heated mainly by the accumulation of numerous nanoflares coming from reconnection events and by magnetoacoustic shocks.

Observations with instruments such as *TRACE* (Krucker & Benz 1998; Parnell & Jupp 2000) and *Yohkoh* SXT (Katsukawa & Tsuneta 2001) have shown that nanoflares in the corona are rather impulsive and ubiquitous in character thus supporting the nanoflare reconnection scenario. The intermittent behavior of coronal loops, and their modeling by random energy deposition representing nanoflares of locally damped wave heating, was studied by Mendoza-Briceño et al. (2002, 2005) and Mendoza-Briceño & Erdélyi (2006). However, Moriyasu et al. (2004) showed that the observed spiky intensity profiles due to impulsive releases of energy could also be specifically obtained from nonlinear Alfvén wave heating. It was found that Alfvén waves can nonlinearly convert into slow and fast magnetoacoustic modes which then steepen into shocks and heat the plasma to coronal temperatures balancing losses due to thermal conduction and radiation. The shock heating due to the conversion of Alfvén waves was found to be episodic, impulsive, and uniformly distributed throughout the corona, producing an X-ray intensity profile that matches observations. Hence, Moriyasu et al. (2004) proposed that the observed nanoflares may not be directly related to reconnection but rather to Alfvén waves.

[1] Also at: The Institute of Theoretical Astrophysics, University of Oslo, P.O. Box 1029, Blindern, NO-0315 Oslo, Norway.
[2] Also at: George Mason University, 4400 University Drive, Fairfax, VA 22020.

It has been shown that energy release processes in the Sun, from solar flares down to microflares, follow a power-law distribution in frequency with an index (slope) around -1.6 (Shimizu 1995). Hudson (1991) showed that if smaller energetic events such as nanoflares have a power-law distribution with an index steeper than -2 then they would represent the bulk of the heating in the corona. Measurements of this quantity have, however, shown a large range of values (cf. Table 1 in Benz & Krucker 2002; Aschwanden 2004).

In Taroyan et al. (2007) it has been shown that an analysis of power spectra of Doppler shift time series allows to differentiate between uniformly heated loops from loops heated near their footpoints. Taking into account the uniform heating nature resulting from Alfvén waves (Moriyasu et al. 2004) this idea could also allow us to differentiate Alfvén wave heated loops from loops heated by mechanisms concentrating the heating toward the footpoints. Following this idea, in this work we propose a way to discern observationally between Alfvén wave heating and nanoflare reconnection heating. Our idea also constitutes a diagnostic tool for the location of the heating along coronal loops. It relies on the fact that the distribution of the shocks in loops differs substantially between the two models, due to the different characteristics of the wave modes they produce. As a consequence, X-ray intensity profiles differ substantially between an Alfvén wave heated corona and a nanoflare heated corona. The frequency distribution of the heating events obtained from the intensity profile is found to follow a power-law distribution in both cases, with indexes (slopes) which differ significantly from one heating model to the other, depending also on the "observed" region of the magnetic flux tube. We thus analyze the link between the power-law index of the frequency distribution and the operating heating mechanism in the loop. We also predict different flow structures and different average plasma velocities along the loop depending on the heating mechanism and on its spatial distribution.

The article is organized as follows. We start by setting up the two heating models (§ 2) applied to a coronal loop. Following Moriyasu et al. (2004) the first model consists of Alfvén waves that are generated at the footpoints of the magnetic flux tube due to random perturbations simulating convective motions. The second model consists of heating events with nanoflare-like energies (simulating reconnection events) that are randomly distributed, either throughout the loop or concentrated at the footpoints. As in Moriyasu et al. (2004) the loops are modeled with a 1.5-dimensional (1.5D) MHD code including thermal conduction and radiative cooling. The evolution of the loops is analyzed in § 3, and in § 4 we construct observables like the intensity profiles along the loops and discuss the results. Conclusions are presented in § 5.

2. MODELS

2.1. *Geometry of the Loop and MHD Equations*

The model is essentially the same as in Moriyasu et al. (2004). It consists of a magnetic flux tube (loop) of 100 Mm in length whose geometry takes into account the predicted expansion of magnetic flux in the photosphere and chromosphere, displaying an apex-to-base area ratio of 1000. We take the local curvilinear coordinates (s, ϕ, and r) where s measures distance along the most external poloidal magnetic field line, ϕ is the azimuthal angle measured around the rotation axis of the flux tube, and r is the radius of the tube (cf. Fig. 1). We take the 1.5D approximation,

$$\frac{\partial}{\partial \phi} = 0, \quad \frac{\partial}{\partial r} = 0, \quad v_r = 0, \quad B_r = 0, \tag{1}$$

where v_r and B_r are, respectively, the radial components of the velocity and magnetic field in the magnetic flux tube. Hence, although torsional motions are allowed, the shape of the loop does not change. In the considered approximation, conservation of magnetic flux defines the value of the poloidal magnetic field as a function of r alone, $B_s = B_0(r_0/r)^2$, where B_0 is the value of the magnetic field at the photosphere and $r_0 = 200$ km is the initial radius of the loop. In the photosphere the value of $\beta = 8\pi p/B_s^2$ (the ratio of gas to magnetic pressures) is unity. We assume an inviscid perfectly conducting fully ionized plasma. The effects of thermal conduction and radiative cooling are considered.

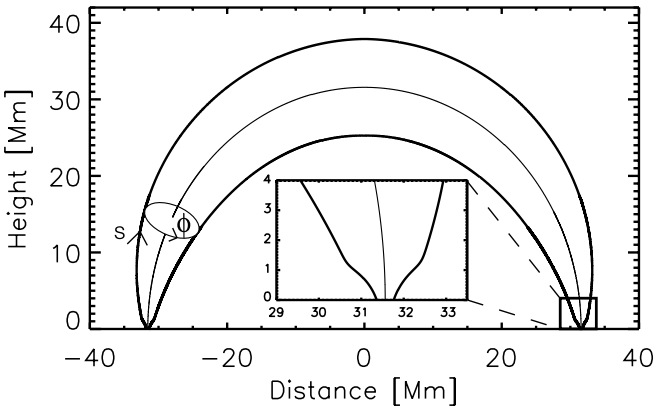

FIG. 1.— Geometry of the loop. The length of the loop is 100 Mm and the apex-to-base ratio of the area cross section is 1000.

The 1.5D MHD equations are written as follows. The mass conservation equation:

$$\frac{\partial \rho}{\partial t} + v_s \frac{\partial \rho}{\partial s} = -\rho B_s \frac{\partial}{\partial s}\left(\frac{v_s}{B_s}\right); \tag{2}$$

the s-component of the momentum equation:

$$\frac{\partial v_s}{\partial t} + v_s \frac{\partial v_s}{\partial s} = -\frac{1}{\rho}\frac{\partial p}{\partial s} - g_s + \frac{v_\phi^2}{r}\frac{\partial r}{\partial s} - \frac{1}{4\pi\rho}\frac{B_\phi}{r}\frac{\partial}{\partial s}(rB_\phi); \tag{3}$$

the ϕ-component of the momentum equation:

$$\frac{\partial (rv_\phi)}{\partial t} + v_s \frac{\partial (rv_\phi)}{\partial s} = \frac{B_s}{4\pi\rho}\frac{\partial}{\partial s}(rB_\phi) + \mathcal{C}(t,s); \tag{4}$$

the induction equation:

$$\frac{\partial}{\partial t}\left(\frac{B_\phi}{rB_s}\right) + \frac{\partial}{\partial s}\left(\frac{B_\phi}{rB_s}v_s - \frac{v_\phi}{r}\right) = 0; \tag{5}$$

and the energy equation:

$$\frac{\partial e}{\partial t} + v_s \frac{\partial e}{\partial s} = -(\gamma - 1)eB_s \frac{\partial}{\partial s}\left(\frac{v_s}{B_s}\right) - \frac{R - \mathcal{S} - \mathcal{H}}{\rho} + \frac{1}{\rho r^2}\frac{\partial}{\partial s}\left(r^2 \kappa \frac{\partial T}{\partial s}\right); \tag{6}$$

where

$$p = \rho \frac{k_B}{m} T, \quad e = \frac{1}{\gamma - 1}\frac{p}{\rho}. \tag{7}$$

In the above equations(2)–(6) ρ, p, and e are, respectively, density, pressure, and internal energy; v_s is the poloidal component of the velocity along the external magnetic field line; v_ϕ is the toroidal (azimuthal) component of the velocity; B_s and B_ϕ are,

respectively, the poloidal and toroidal components of the magnetic field; k_B is the Boltzmann constant, and γ is the ratio of specific heats for a monatomic gas, taken to be 5/3. The g_s is the effective gravity along the external poloidal magnetic field line and is given by

$$g_s = g_\odot \cos\left(\frac{z}{L}\pi\right)\frac{dz}{ds}, \tag{8}$$

where $g_\odot = 2.74 \times 10^4$ cm s^{-2} is the gravity at the base of the loop, z is the length along the central axis of the loop, and L is the total length of the loop. The $\mathcal{C}(t, s)$ in equation (4) is a term considered only in the Alfvén wave heating model which simulates the torque motions in the photosphere. It is responsible for the generation of Alfvén waves,

$$\begin{aligned}\mathcal{C}(t,s) = {} & 2r(s)[\mathrm{rand1}(t) - 0.5] f\left[\tanh\left(\frac{s - 0.55H_0}{0.055H_0}\right) - 1\right] \\ & + 2r(s)[\mathrm{rand2}(t) - 0.5] \\ & \times f\left[\tanh\left(\frac{L - s - 0.55H_0}{0.055H_0}\right) - 1\right].\end{aligned} \tag{9}$$

Here H_0 denotes the pressure scale height at $z = 0$. We take $H_0 = 200$ km. The terms rand1(t) and rand2(t) are noncorrelated functions that output a number randomly distributed between 0 and 1, which changes in time, and f is a parameter that determines the strength of the torque. The spectrum of the Alfvén waves generated in the photosphere that issue from these perturbations corresponds to white noise. Due to the random buffeting of magnetic field lines by turbulent motions from convection it is reasonable to expect a wide range of frequencies for the generated Alfvén waves, which would justify the choice of this approach. It is nonetheless interesting to locate which is the frequency range which is most appropriate for the heating of the corona in the present case. To answer this question we also perform simulations with photospheric perturbations which generate specific monochromatic spectra for the Alfvén waves. In equation (6), $\kappa = 9 \times 10^{-7}$ erg s^{-1} K^{-1} cm^{-1} is the Spitzer conductivity corresponding to a fully ionized plasma. Here $\mathcal{S}$ is a heating term maintaining the initial temperature distribution of the loop. The radiative losses $R(T)$ are defined as

$$R(T) = n_e n_p Q(T) = \frac{n^2}{4} Q(T), \tag{10}$$

where $n = n_e + n_p$ is the total particle number density (n_e and n_p are, respectively, the electron and proton number densities, and we assume $n_e = n_p = \rho/m$ to satisfy plasma neutrality, with m the proton mass) and $Q(T)$ is the radiative loss function for optically thin plasmas (Landini & Monsignori Fossi 1990), which is approximated with analytical functions of the form $Q(T) = \chi T^\gamma$. We take the same approximation as in Hori et al. (1997; please refer to their Table 1). For temperatures below 4×10^4 K we assume that the plasma becomes optically thick. In this case, the radiative losses R can be approximated by $R(\rho) = 4.9 \times 10^9 \rho$ (Anderson & Athay 1989). In equation (6) the heating term $\mathcal{S}$ has a constant nonzero value which is nonnegligible only when the atmosphere becomes optically thick. Its purpose is mainly for maintaining the initial temperature distribution of the loop. Here $\mathcal{H}$ denotes the nanoflare heating function and is described in the following section. It is not taken into account in the Alfvén wave heating model.

2.2. *Nanoflare Heating Model*

Hydrodynamic modeling of nanoflare heating has already been done in the past (Walsh et al. 1997; Cargill & Klimchuk 2004; Patsourakos & Klimchuk 2005; Taroyan et al. 2006; Mendoza-Briceño et al. 2005; Spadoro et al. 2003, 2006). The nanoflare model considered here is basically one-dimensional and is similar to the model of Taroyan et al. (2006) with respect to the heating function $\mathcal{H}$ in equation (6). Heating events simulating nanoflares are input randomly throughout the loop as artificial perturbations in the internal energy of the gas. Only slow magnetoacoustic modes are generated in this model. In other words, we suppose that Alfvén waves that may be generated in small reconnection events leading to nanoflares in the corona do not carry a significant amount of energy compared to slow magnetoacoustic waves. The validity of this assumption is still under debate. Parker (1991) suggested a model in which 20% of the energy released by reconnection events in the solar corona is transfered as a form of Alfvén wave. Yokoyama (1998) studied the problem simulating reconnection in the corona, and found that less than 10% of the total released energy goes into Alfvén waves. This result is similar to the 2D simulation results of photospheric reconnection by Takeuchi & Shibata (2001) in which it is shown that the energy flux carried by the slow magnetoacoustic waves is one order of magnitude higher that the energy flux carried by Alfvén waves. On the other hand, recent simulations by H. Kigure et al. (2002, private communication) show that the fraction of Alfvén wave energy flux in the total released magnetic energy during reconnection (nanoflare) may be significant (more than 50%). It would thus be interesting to also consider a case in which a part of the energy from reconnection events goes also into Alfvén waves. This would, however, be the subject of another paper.

The spatial distribution of the heating in coronal loops is a controversial point. Parker's nanoflare model supposes uniformly distributed heating along loops. However, observational evidence not only for uniform heating (Priest et al. 1998) but also for footpoint heating (Aschwanden 2001) has been found. Here we consider nanoflares distributed toward the footpoints ("footpoint heating"; see Mendoza-Briceño et al. 2002), as well as uniformly (randomly) distributed along the loop ("uniform heating"). We adopt the same form of the heating function for each event as in Taroyan et al. (2006). The heating rate due to the nanoflares is represented as

$$\mathcal{H} = \sum_{i=1}^{n} \mathcal{H}_i(t, s), \tag{11}$$

where $\mathcal{H}_i(t, s)$, $i = 1, \ldots, n$ are the discrete episodic heating events, and n is the total number of events;

$$\mathcal{H}_i(t,s) = \begin{cases} E_0 \sin\left[\dfrac{\pi(t - t_i)}{\tau_i}\right] \exp\left(-\dfrac{|s - s_i|}{s_h}\right), & t_i < t < t_i + \tau_i, \\ 0, & \text{otherwise}, \end{cases} \tag{12}$$

where E_0 is the maximum volumetric heating and s_h is the heating scale length. The offset time t_i, the maximum duration τ_i, and the location s_i of each event are randomly distributed in the following ranges:

$$t_i \in [0, t_{\mathrm{total}}], \tau_i \in [0, \tau_{\max}], \tag{13}$$

$$s_i \in \begin{cases} [s_{\min}, L - s_{\min}], & \text{(uniform)} \\ [s_{\min}, s_{\max}] \bigcup [L - s_{\max}, L - s_{\min}], & \text{(footpoint)} \end{cases}, \tag{14}$$

where $t_{\rm total}$ is the total simulation time, $s_{\rm min}$ ($s_{\rm max}$) define the lower (upper) boundaries of the range in the loop where heating events occur, and "uniform" ("footpoint") denotes uniform (footpoint concentrated) heating. Integrating in time and space (eq. [12]) and considering the cross-section area where the heating occurs we can calculate the mean total energy $\mathcal{E}$ per event,

$$\mathcal{E} = \left\langle \int_0^L \int_{t_i}^{t_i+\tau_i} A(s)\mathcal{H}_i(t,s)\,dt\,ds \right\rangle \simeq \frac{4}{\pi} s_h \langle A\rangle \langle \tau_i\rangle \langle E_0\rangle, \quad (15)$$

where brackets denote the mean value of the quantity. In the integration, the area has been taken out, and replaced by its mean value in the region where the heating events occur. This is justified considering that most of the expansion occurs close to the footpoints, below the location of the heating events. Apart from the spatial distribution, we consider two different kinds of energy distribution. The first kind has the maximum volumetric energy per event, E_0, as constant, hence defining a uniform distribution in energies for the events:

$$\mathcal{E} = \frac{2}{\pi} s_h \langle A\rangle \tau_{\rm max} E_0. \quad (16)$$

The corresponding mean energy flux $\mathcal{F}$ for this case is

$$\mathcal{F} \simeq \frac{n\mathcal{E}}{t_{\rm total}\langle A\rangle} = \frac{2ns_h\tau_{\rm max}E_0}{\pi t_{\rm total}}. \quad (17)$$

The second kind has the volumetric energies E_0 of the events distributed as a power law. The reason behind this choice is the observational fact that energy release processes in the corona, from solar flares down to microflares, follow a power-law distribution in frequency with an index (slope) of about $\delta = -1.6$ (Shimizu 1995). The probability density function of the volumetric heating E_0 in this case is then

$$\frac{dN(E_0)}{dE_0} = \frac{1+\alpha}{E_{\rm max}^{(1+\alpha)} - E_{\rm min}^{(1+\alpha)}} E^{\alpha} \quad \text{for} \quad E_0 \in [E_{\rm min}, E_{\rm max}], \quad (18)$$

where $N(E_0)$ is the number of heating events having a volumetric energy between E_0 and $E_0 + dE_0$, $E_{\rm min}$ and $E_{\rm max}$ are, respectively, the smallest and the biggest allowed volumetric energy for the events, and α is the power-law index of the distribution.[3] Hence, the mean total energy per event results,

$$\mathcal{E} = \frac{2}{\pi} s_h \langle A\rangle \tau_{\rm max} \int_{E_{\rm min}}^{E_{\rm max}} E_0 \frac{dN(E_0)}{dE_0}\,dE_0 = \frac{2}{\pi}\tau_{\rm max} s_h \langle A\rangle \left(\frac{1+\alpha}{2+\alpha}\right) \frac{E_{\rm max}^{(2+\alpha)} - E_{\rm min}^{(2+\alpha)}}{E_{\rm max}^{(1+\alpha)} - E_{\rm min}^{(1+\alpha)}}. \quad (19)$$

The mean energy flux in this case is

$$\mathcal{F} = \frac{2n\tau_{\rm max}s_h}{\pi T}\left(\frac{1+\alpha}{2+\alpha}\right) \frac{E_{\rm max}^{(2+\alpha)} - E_{\rm min}^{(2+\alpha)}}{E_{\rm max}^{(1+\alpha)} - E_{\rm min}^{(1+\alpha)}}. \quad (20)$$

In order to produce in the simulation heating events having energies with the power-law distribution in frequency written in equation (18), we start with a random (uniform) distribution of values x in [0,1], to which we apply the following transformation:

$$E_0(x) = \left\{ E_{\rm min}^{(1+\alpha)} + \left[E_{\rm max}^{(1+\alpha)} - E_{\rm min}^{(1+\alpha)} \right] x \right\}^{1/(1+\alpha)}. \quad (21)$$

Both cases $\alpha > -2$ and $\alpha < -2$ are considered.

In order to set the values to the parameters of the heating function, equations(12)–(14), an estimate of the nanoflare duration time is needed. One of the hardest parameters to estimate in magnetic reconnection theory is the thickness of the current sheet, i.e., the length across the reconnection region. If this parameter is of the order of ~1000 km, the timescale of a (small) reconnection event leading to a nanoflare should oscillate between 1 and 10 s, since the order of the Alfvén speed in the chromosphere and in the corona is, respectively, ~100 and ~1000 km s^{-1}. This value, however, is not established. In the present work we consider runs with maximum duration times for a heating event of $\tau_{\rm max} = 10$ and 40 s. The heating scale length is also allowed to vary: runs with $s_h = 200$, 500, or 1000 km are considered. The frequency of the heating events can be 1/50, 1/34, or 1/7 s^{-1}. For footpoint-concentrated heating the events are randomly distributed in the loop range defined by $\{s_{\rm min} = 2, s_{\rm max} = 20\}$ Mm, $\{s_{\rm min} = 2, s_{\rm max} = 12\}$ Mm, or $\{s_{\rm min} = 1, s_{\rm max} = 10\}$ Mm (see eq. [14]). For uniform heating along the loop we take $s_{\rm min} = 2$ Mm. For runs with uniformly distributed energies we take $E_0 = 0.01, 0.05$, or 0.5 erg cm^{-3} s^{-1}. For runs with energies that follow a power-law distribution in frequencies we take $E_{\rm min} = 0.005$ erg cm^{-3} s^{-1} and $E_{\rm max} = 10$ erg cm^{-3} s^{-1}. Several values for the power-law index α are tried, ranging from -1.5 to -2.2. Using equations (16), (17), (19), and (20) we calculate in Table 1 the extremum values among the runs for the mean energy per event and for the mean energy flux.

2.3. *Initial Conditions and Numerical Code*

The present model differs from the model of Moriyasu et al. (2004) in that a subphotospheric region is considered by adding 2 Mm at each footpoint of the loop, in which the radius of the loop is kept constant (hence keeping a constant magnetic flux). We take the origin $s = z = 0$ as the top end of this region. The loop is assumed to follow hydrostatic pressure balance in the subphotospheric region and in the photosphere up to a height of $4H_0 = 800$ km, where H_0 is the pressure scale height at $z = 0$. The inclusion of the subphotospheric region avoids unrealistic density oscillations due to the reflection of waves at the boundaries, thus avoiding any influence from the boundary conditions on the coronal dynamics. For the rest of the loop, density decreases as $\rho \propto h^{-4}$, where h is the height from the base of the loop. This is based on the work by Shibata et al. (1989a, 1989b) in which the results of 2D MHD simulations of emerging flux by Parker instability exhibit such pressure distribution. The initial temperature all along the loop is set at $T = 10^4$ K. The density at the photosphere ($z = 0$) is set at $\rho_0 = 2.53 \times 10^{-7}$ g cm^{-3}, and, correspondingly, the photospheric pressure is $p_0 = 2.09 \times 10^5$ dyn cm^{-2}. As the plasma β parameter is chosen to be unity in the photosphere, the value adopted for the magnetic field at $z = 0$ is $B_0 = 2.29 \times 10^3$ G. The value of the magnetic field at the top of the loop is then $B_{s,\rm top} = 2.29$ G.

In Moriyasu et al. (2004) the spatial resolution in the numerical scheme was taken to be 20 km throughout the loop. In order to better resolve the dynamics in the chromosphere and transition region here we improve the spatial resolution by taking a grid size of $\Delta s = 0.025H_0 = 5$ km up to a height of ~16,000 km. Then, the grid size increases as $\Delta s_{i+1} = 1.03\Delta s_i$ until it reaches

[3] The power-law index α of the distribution of the energies of the events is to be distinguished from δ, the measured power-law index from observations. These two quantities can indeed be different as is shown in § 4.

TABLE 1
MEAN INPUT VALUES FOR THE NANOFLARE MODEL

Event Distribution (1)	Energy Distribution (2)	Number of Runs (3)	⟨Energy⟩ Min–Max (erg) (4)	⟨Flux⟩ Min–Max (erg cm^{-2} s^{-1}) (5)
Loop	Uniform	4	8.2×10^{24}–8.2×10^{26}	2.5×10^{5}–2.5×10^{7}
Footpoint	Uniform	10	1.3×10^{23}–4.7×10^{26}	4.7×10^{5}–2.5×10^{7}
Loop	Power law	4	9.3×10^{24}–2.9×10^{25}	2.1×10^{6}–6.6×10^{6}
Footpoint	Power law	10	4.9×10^{24}–2.2×10^{25}	4.8×10^{6}–2.1×10^{7}

NOTES.—Col. (1): Spatial distribution of the heating, either uniformly distributed along the loop ("loop") or concentrated at the footpoints ("footpoint"). The energy distribution among the events can be uniform or can follow a power law with a certain index, corresponding, respectively, to "uniform" and "power law" (col. [2]). Col. (3): Number of runs performed with such heating distribution. Cols. (4) and (5): Extremum values among the runs for the mean energy per event and for the mean energy flux, respectively (minimum and maximum).

a size of 20 km. The size is then kept constant up to the apex of the loop. The total grid number is 10,800. We take rigid wall boundary conditions at the photosphere. The numerical schemes adopted are the CIP scheme (Yabe & Aoki 1991) and the MOC-CT scheme (Evans & Hawley 1988; Stone & Norman 1992). Please refer to Kudoh et al. (1998) for details about the application of these schemes. The total time of the simulation is 568 minutes.

3. NUMERICAL RESULTS

3.1. *From Nonlinear Alfvén Waves*

In the present case we adopt a photospheric driver producing a white noise frequency spectrum for the Alfvén waves, which we consider simulates to a certain extent the turbulent motions in the photosphere. It is however interesting to locate the range of frequencies for the Alfvén waves which is the most ideal for coronal heating under the considered heating mechanism (mode conversion). As shown by Musielak et al. (2007) torsional Alfvén waves have cutoff-free propagation along thin magnetic flux tubes. In the present case, however, the flux tube presents a density stratification which introduces a frequency cutoff. According to Noble et al. (2003), typical values for these cutoffs oscillate between 100 and 300 s. On the other hand, high-frequency waves are rapidly damped when propagating through the lower atmospheric layers. In Table 2 we show values for the average temperature in the corona obtained with a monochromatic driver in the photosphere generating the Alfvén waves. We consider waves with 10, 25, 50, 100, 150, and 300 s periods, each with different amplitudes. In the table we show the results for amplitudes of the driver resulting in a $\langle v_\phi^2\rangle^{1/2} \sim 1.1$ km s^{-1} azimuthal velocity field at the photosphere. The results seem to indicate that the range of waves with periods between 100 and 150 s is the most favorable for the real solar corona. Larger period waves seem to suffer from the frequency cutoff. In the following results concerning Alfvén wave heating we employ the photospheric driver producing the white noise spectrum discussed in § 2.1.

The left panels of Figure 2 show the profiles at times $t =$ 0 minutes (*dotted line*), $t = 33.5$ minutes (*dashed line*), and $t =$ 270.7 minutes (*solid line*) of the temperature, density, poloidal velocity, and the ratio of the toroidal (azimuthal) and poloidal components of the magnetic field for a typical case of a loop heated by Alfvén waves. We present here a case in which the photospheric driver producing the waves generates a photospheric velocity field with $\langle v_\phi^2\rangle^{1/2} = 1.6$ km s^{-1}. The evolution from $t =$ 300 to 360 minutes can be appreciated in the panels of Figures 3 where (*a*) temperature, (*b*) poloidal velocity, (*c*) pressure, and (*d*) density are displayed. As shown in Kudoh & Shibata (1999) and in Moriyasu et al. (2004), due to nonlinear effects Alfvén waves convert to longitudinal slow and fast modes when propagating from the photosphere to the chromosphere which then steepen into slow and fast shocks, respectively. Mode conversion and the subsequent shock formation also happens everywhere in the corona. This can be understood from Figure 2 (*bottom*) which shows the ratio B_ϕ/B_s of the toroidal (azimuthal) component to the poloidal component of the magnetic field. This quantity becomes high episodically, not only in the chromosphere but also in the corona. When this happens nonlinear effects are large and energy is transfered from the Alfvén mode to the longitudinal slow and fast modes, which steepen into shocks and heat the plasma. The heating from the shocks is episodic and uniformly distributed throughout the corona. This can be seen in Figure 3*a* where bright features with temperatures close to 2 MK have elongated shapes throughout the corona corresponding to the traces of the strong shocks that heat the plasma (the traces are clearly seen in all panels of Fig. 3). The loop gradually heats from chromospheric to coronal temperatures, the coronal part of the loop increasing in length and becoming flatter with time due to the uniformly distributed shock heating and to thermal conduction. After $t = 150$ minutes approximately, the loop reaches a quasi-steady state in which radiative losses, thermal conduction and shock heating are in balance. As shown in Moriyasu et al. (2004) Alfvén wave heated loops satisfy the RTV scaling law (Rosner et al. 1978). The obtained overall nonflat temperature profile is characteristic of uniformly heated loops, as described by Priest et al. (1998) from X-ray observations of the diffuse corona. Although in a steady state, the emerging corona is characterized by a highly dynamical state, with flow velocities in the corona reaching 150 km s^{-1} at various times (Fig. 3*b*), which is one of the most interesting features of this model. The transition region is highly dynamical, as shown by panels *a* and *d*. The potential of the Alfvén wave

TABLE 2
AVERAGE CORONAL TEMPERATURE FOR MONOCHROMATIC ALFVÉN WAVES

Period (s)	Temperature (MK)
10	0.29
25	0.63
50	0.74
100	1.18
150	1.26
300	0.91

NOTES.—Alfvén wave heating resulting from a monochromatic photospheric driver. We show the average temperature in the corona resulting from shock heating from mode conversion of monochromatic torsional Alfvén waves generated in the photosphere. We consider waves with 10, 25, 50, 100, 150, and 300 s periods. The amplitudes of the driver are such that a $\langle v_\phi^2\rangle^{1/2} \sim 1.1$ km s^{-1} azimuthal photospheric velocity field is generated.

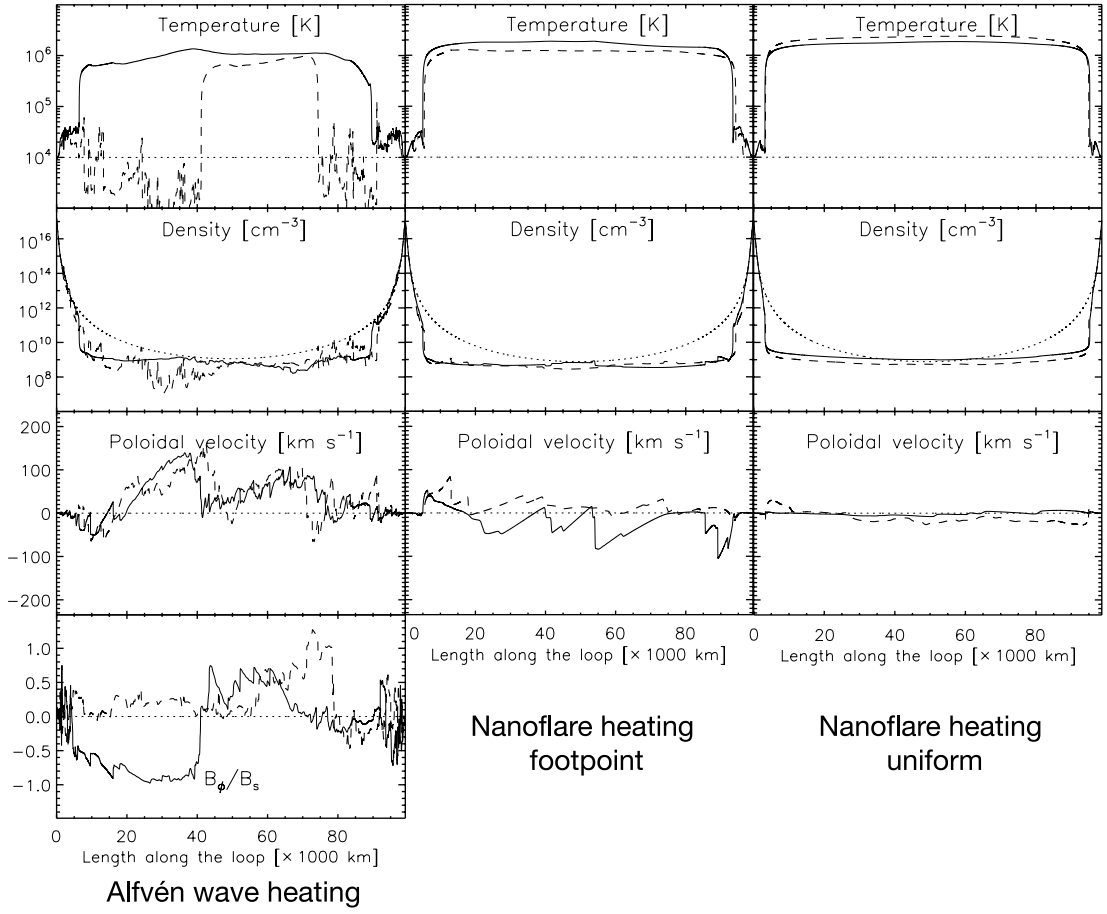

FIG. 2.—Profiles of quantities along the loop at various times for a loop heated by Alfvén waves (*left panels*), and a loop with heating events simulating nanoflares concentrated at the footpoints (*center panels*) or uniformly distributed along its length (*right panels*). In the case of Alfvén wave heating, the Alfvén waves are generated by a photospheric velocity field of $\langle v_\phi^2 \rangle^{1/2} = 1.6$ km s^{-1}. Rows indicate, from top to bottom, respectively, profiles along the loop for temperature, density, and poloidal velocity. The bottom left panel shows the toroidal to poloidal magnetic field ratio for the case where Alfvén waves are present. The profiles are plotted for $t = 0$ minutes (*dotted line*), $t = 33.5$ minutes (*dashed line*), and $t = 270.7$ minutes (*solid line*).

model for creating spicules and other chromospheric dynamical events has already been shown (Kudoh & Shibata 1999; James & Erdélyi 2002).

In Moriyasu et al. (2004) and Moriyasu & Shibata (2004) it is shown that when the amplitude of the motions in the photosphere is strong enough so that the photospheric velocity field satisfies $\langle v_\phi^2 \rangle^{1/2} \gtrsim 1$ km s^{-1} a hot corona is created in the loop. Figure 4 shows the mean temperature in the corona with respect to the photospheric rms velocity field created by the torsional motions at the footpoints of the loop in our case. This figure is similar to Figure 4 in Moriyasu & Shibata (2004). The small differences can be attributed to the inclusion of the subphotospheric region which damps most of the incoming wave energy. Also, the present simulation has 4 times better spatial resolution from the subphotosphere to the low corona. The higher spatial resolution allows better treatment of high-frequency waves, which carry most of the energy from the convective layers of the Sun toward the corona, but they dissipate more strongly than low-frequency waves. As a consequence, more energy goes into chromospheric heating and higher energy fluxes from the photosphere are needed for creating and sustaining a corona, shifting toward higher values the necessary photospheric velocity fields. In order to have a corona we must have $\langle v_\phi^2 \rangle^{1/2} \gtrsim 1.3$ km s^{-1} in the present model.

3.2. *From Nanoflares*

In the center and right panels of Figure 2 the time profiles at $t = 0$, 33.5, and 270.7 minutes of the temperature, density, and poloidal velocity along the loop are shown for two typical cases of nanoflare heating. The center panels correspond to a loop whose heating events are concentrated toward the footpoints (in the loop range [2, 12] Mm and [88, 98] Mm). For this run, the mean energy per event is 6.6×10^{24} erg and the mean energy flux is 6.4×10^6 erg cm^{-2} s^{-1}. The right panels correspond to a loop in which heating events are uniformly (randomly) distributed along the loop (in the loop range [2, 98] Mm). The mean energy per event is 4.09×10^{25} erg and the mean energy flux is 1.27×10^6 erg cm^{-2} s^{-1}. In both cases the energy flux deposited by the heating events is enough to heat the loop to coronal values, agreeing with the nanoflare simulation results by Mendoza-Briceño et al. (2002). The evolution from $t = 300$ to 360 minutes is displayed in Figure 5 for the loop with heating events concentrated toward the footpoints, and in Figure 6 for the loop with uniformly distributed heating events. Profiles along the loop of (*a*) temperature, (*b*) poloidal velocity, (*c*) pressure, and (*d*) density are displayed.

Figure 7 shows the mean temperature in the corona with respect to the mean energy flux input from the heating events simulating nanoflares. Squares designate loops which heating events are uniformly (randomly) distributed along their lengths above a height of 2 Mm from the photosphere. All other symbols designate loops with heating events concentrated toward the footpoints. Diamonds correspond to loops with heating events concentrated in the loop ranges defined by $\{s_{\min} = 2, s_{\max} = 20\}$ Mm (see eq. [14]). Triangles are for loops with $\{s_{\min} = 2, s_{\max} = 12\}$ Mm, and crosses are for loops with $\{s_{\min} = 1, s_{\max} = 10\}$ Mm. As expected, the

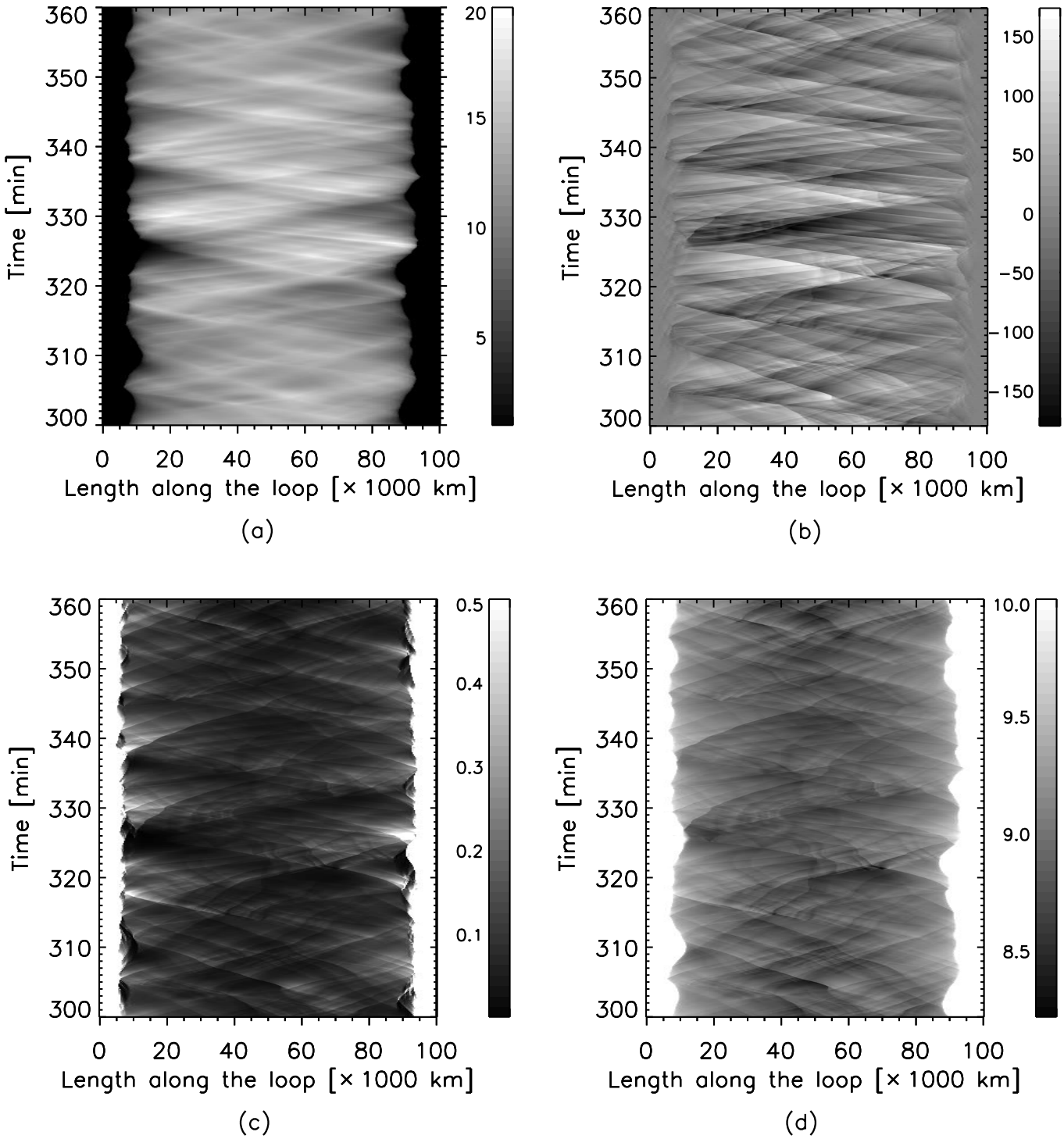

FIG. 3.—Evolution of (*a*) temperature, (*b*) poloidal velocity, (*c*) pressure, and (*d*) density from $t = 300$ to 360 minutes for a loop heated by Alfvén waves generated by a photospheric velocity field of $\langle v_\phi^2 \rangle^{1/2} = 1.6$ km s^{-1}. The temperature, pressure, and density maps are saturated above the specified maximum value.

general trend of a higher mean coronal temperature for a higher energy flux input is present. The more the heating is concentrated toward the footpoints, the less the mean temperature in the corona. This distribution in the plot can be understood by means of thermal conduction. When heating takes place close to the footpoints thermal conduction transports the energy into the corona. Also, closer to the footpoints thermal conduction has lower values. Two coronae receiving the same energy flux will have mean temperatures that relate through their overall heating scale lengths, that is, the range where the heating events occur. For instance, if T_1 and T_2 denote the mean coronal temperatures of two loops with uniform and footpoint concentrated heating respectively (with $\{s_{\min} = 1, s_{\max} = 10\}$ Mm for the latter case), having a same thermal conduction flux implies

$$\frac{T_1}{T_2} \simeq \left(\frac{S_{h1}}{S_{h2}}\right)^{2/7}, \tag{22}$$

where S_h denotes the range where the heating events occur. We have $S_{h1} \simeq 100$ Mm for the uniform heating case, and $S_{h2} \simeq 10$ Mm

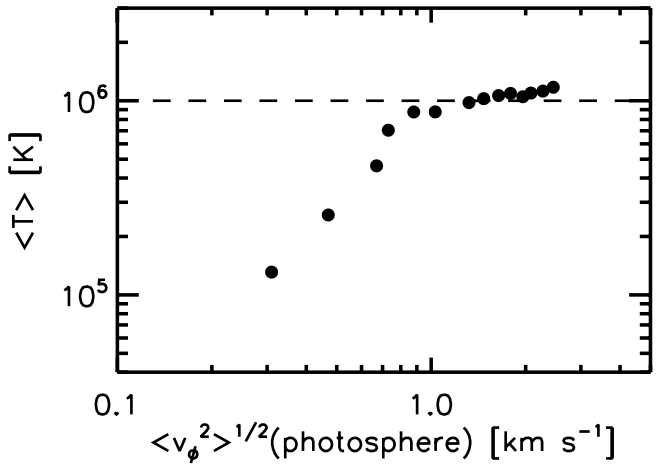

FIG. 4.—Alfvén wave heating. Mean temperature in the corona with respect to the photospheric rms velocity due to the amplitude of the torsional motions at the loop footpoints. We can see that for $\langle v_\phi^2 \rangle^{1/2} \gtrsim 1.3$ km s^{-1} a corona is created.

for the footpoint heating case, implying a temperature ratio of $\sim$2, which corresponds approximately with the separation between squares and crosses in Figure 7.

3.3. *Different Coronal Dynamics*

As discussed at the beginning of § 2.2, the results presented in this section are based on the assumption that during nanoflare reconnection events in the corona the fraction of Alfvén wave energy flux in the total released magnetic energy can be neglected when compared to the energy flux carried by the slow magnetoacoustic waves. A scenario in which this is not the case will be considered in a forthcoming paper.

A heating event produces a local increase in pressure which propagates as an acoustic wave. The traces of these waves, and of corresponding acoustic shocks, show up in the panels of Figures 5 and 6 as bright features, indicating, for instance, high temperatures close to 3 MK. Contrary to the Aflvén wave model, in this case the heating events create sporadic bumps in the temperature profile which are, however, rapidly flattened by thermal conduction. As already pointed out by Mendoza-Briceño et al. (2005), the local bumpy profiles close to the transition region may resemble the intermittent behavior reported by Patsourakos & Vial (2002) from an analysis of light curves from the transition region and low coronal lines, simultaneously recorded in a quiet Sun region by *SOHO* SUMER. When heating events are concentrated toward the footpoints the resulting overall temperature profile is flat, as seen in Figure 2. This agrees with *TRACE* observations of loops being isothermal along their coronal parts (Aschwanden et al. 2001). Figures 2, 5, and 6 show that shocks produced by heating events in the nanoflare models are weaker than shocks produced by Alfvén waves. For footpoint concentrated heating we have strong shocks basically only near the location of the heating events, close to the transition region, as shown by the (*c*) pressure and (*d*) density panels of Figure 5. By the time they reach the apex most of the shocks have dissipated most of their energy. Contrary to the Alfvén wave model where magnetic pressure is also present, the gas pressure from the strong shocks in the nanoflare model is not enough to produce spicules. Heating events occur frequently above the transition region pushing it downwards. Due to the high frequency with which they occur (one to 10 events per minute) the loop reaches a thermal equilibrium in which the transition region is at a relatively low height compared with the Alfvén wave model ($\sim$5000 km for the loop of Fig. 2, *center panels*) with no spicule formation. This is also obtained for the loop with uniformly distributed nanoflares. For this case shocks are weak everywhere. This is due to the higher coronal temperatures that can be achieved with uniform heating (for the same energy flux input), which make flattening of shocks from thermal conduction much more effective. The large difference of the nanoflare heating models with the Alfvén wave heating model is basically due to the combination of two effects: the nonlinear conversion from Alfvén waves to longitudinal slow and fast modes occurs everywhere along the corona, resulting in ubiquitous strong shocks. Also, fast shocks resulting from this conversion dissipate with much less efficiency than slow shocks, which are the only shocks present in the nanoflare model. Hence, strong fast shocks will remain strong shocks for larger times, making a more dynamical corona.

Dynamics can be a good discriminator for coronal heating mechanisms. Indeed, the resulting dynamics from the three heating models (Alfvén wave heating, nanoflare uniform heating, and nanoflare footpoint heating) are quite different. This is shown by Figures 3*b*, 5*b*, and 6*b*. The ubiquitous slow and fast shocks in the Alfvén wave heating model create a many velocity scales flow pattern lacking uniformity, in which flows from one footpoint to the other are hard to trace. We have alternating flows in time from one footpoint to the other creating zigzag shapes in Figure 3*b*. On the other hand, nanoflare heating models create a more uniform flow pattern in which the traces of flows appear clearer. Mostly when the heating events are concentrated toward the footpoints, plasma flows rather simultaneously from one footpoint to the other tending to cross at the apex, creating X shapes in Figures 5*b* and 6*b*.

Average flow velocities in the nanoflare heating cases are not as high as in the Alfvén wave heating case. With the exception of the occasional occurrence of microflares close to the footpoints, which produce the highest temperatures and flow speeds higher than 200 km s^{-1}, nanoflare heating concentrated toward the footpoints produces flows with average velocities of $\sim$15 km s^{-1}. On the other hand Alfvén wave heating produces flows with average velocities of $\sim$50 km s^{-1}. Figures 3*b* and 5*b* show that the footpoint nanoflare heating model has the highest velocities located near the top of the transition region where the heating events take place, whereas for the Alfvén wave heating model these can be found everywhere in the corona. Loops with uniformly distributed heating events show low dynamics, with flow velocities of 5 km s^{-1} in average, as shown by Figure 6.

In the footpoint-concentrated heating case dynamics are occasionally created by the loss of thermal equilibrium in the corona. Indeed, it has been shown that a loop subject to heating concentrated at the footpoints can become thermally unstable at the apex, radiative losses overwhelming the energy flux from thermal conduction (Antiochos et al. 1999; Müller et al. 2003; Mendoza-Briceño et al. 2005). This phenomenon has been termed "catastrophic cooling" and has been proposed as an explanation for coronal rain, which are observations in Hα, or other chromospheric lines, of cool condensations in a hot environment falling down along coronal loops. In the run corresponding to Figure 5 catastrophic cooling occurs two times during the entire simulation. The decrease in temperature and pressure in the corona that follows a catastrophic cooling event drives very rapid plasma flows reaching 100 km s^{-1} and strong shocks in the corona. Coronal rain will be the subject of a future paper.

4. PREDICTING OBSERVABLE FEATURES

4.1. *Intensity Flux Distributions and Intensity Histograms*

We now express the results in terms of observable quantities. We construct the intensity flux profiles and intensity histograms

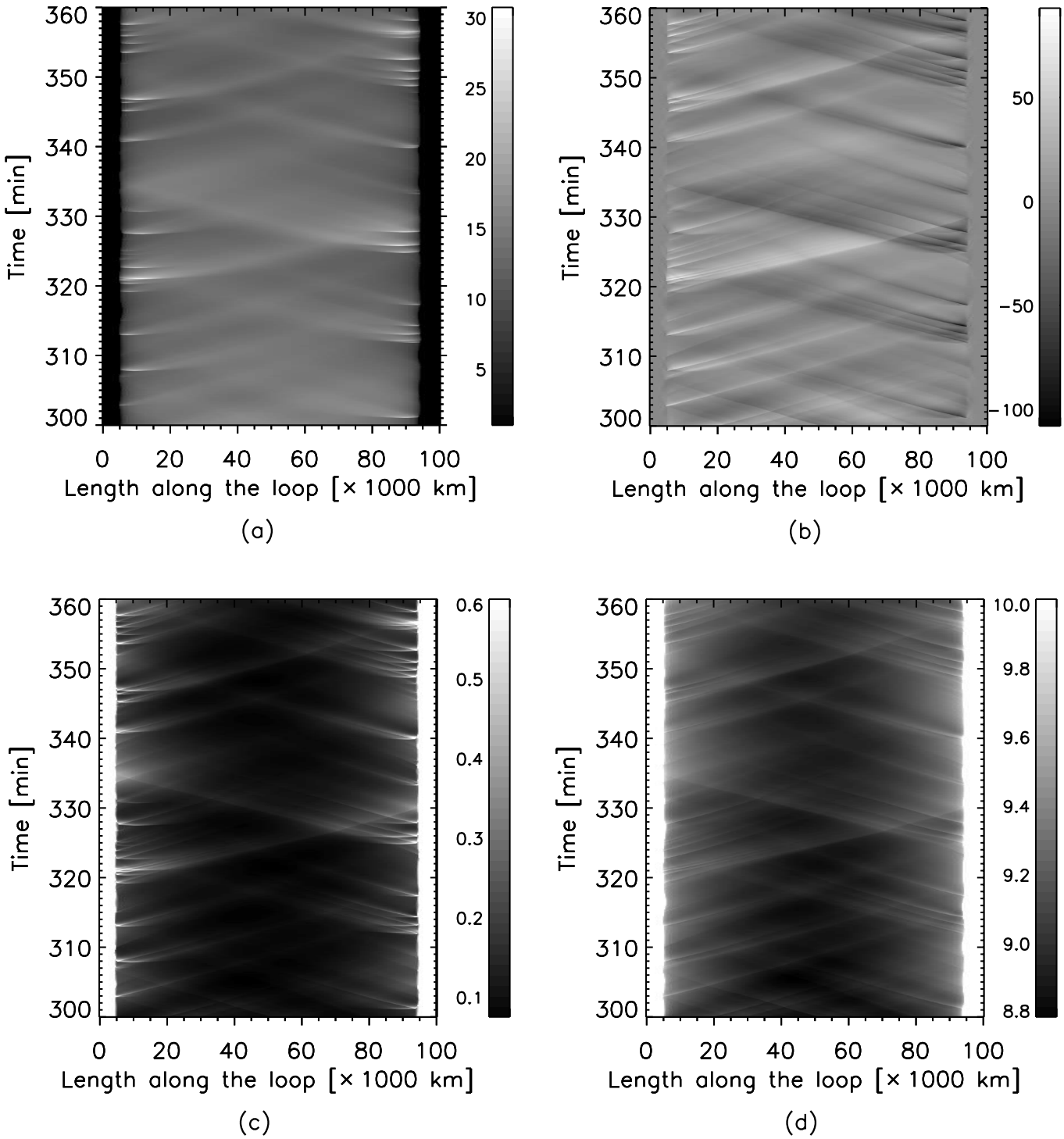

FIG. 5.— Evolution of (*a*) temperature, (*b*) poloidal velocity, (*c*) pressure, and (*d*) density from $t = 300$ to 360 minutes for a loop with heating events concentrated at the footpoints. The temperature, pressure, and density maps are saturated above the specified maximum value.

with the help of *Hinode* XRT response function (using the thin Al mesh filter; please refer to Golub et al. [2007] for details on the *Hinode* XRT). We are thus simulating to a certain extent what *Hinode* XRT would observe of such loops. We take a field of view of $1'' \times 1''$ and we assume that we are observing at the loop from the side (i.e., we assume the loop is at the limb). Figure 8 shows time series of the intensity flux calculated at the top of one of the two transition regions (*top panels*) and at the apex of the loop (*bottom panels*). The corresponding height is indicated on the top of each panel.[4] From left to right the columns show, respectively, a loop heated by Alfvén waves (same loop as in Fig. 3), a loop with heating events concentrated toward the footpoints having as an input a power-law energy spectrum with an index of $\alpha = -1.8$ (loop with similar hydrodynamic response as the loop in

[4] The height of the transition region in the Alfvén wave heating model is higher than for the nanoflare heating models due to the slow and fast MHD shocks that constantly push the transition region upwards.

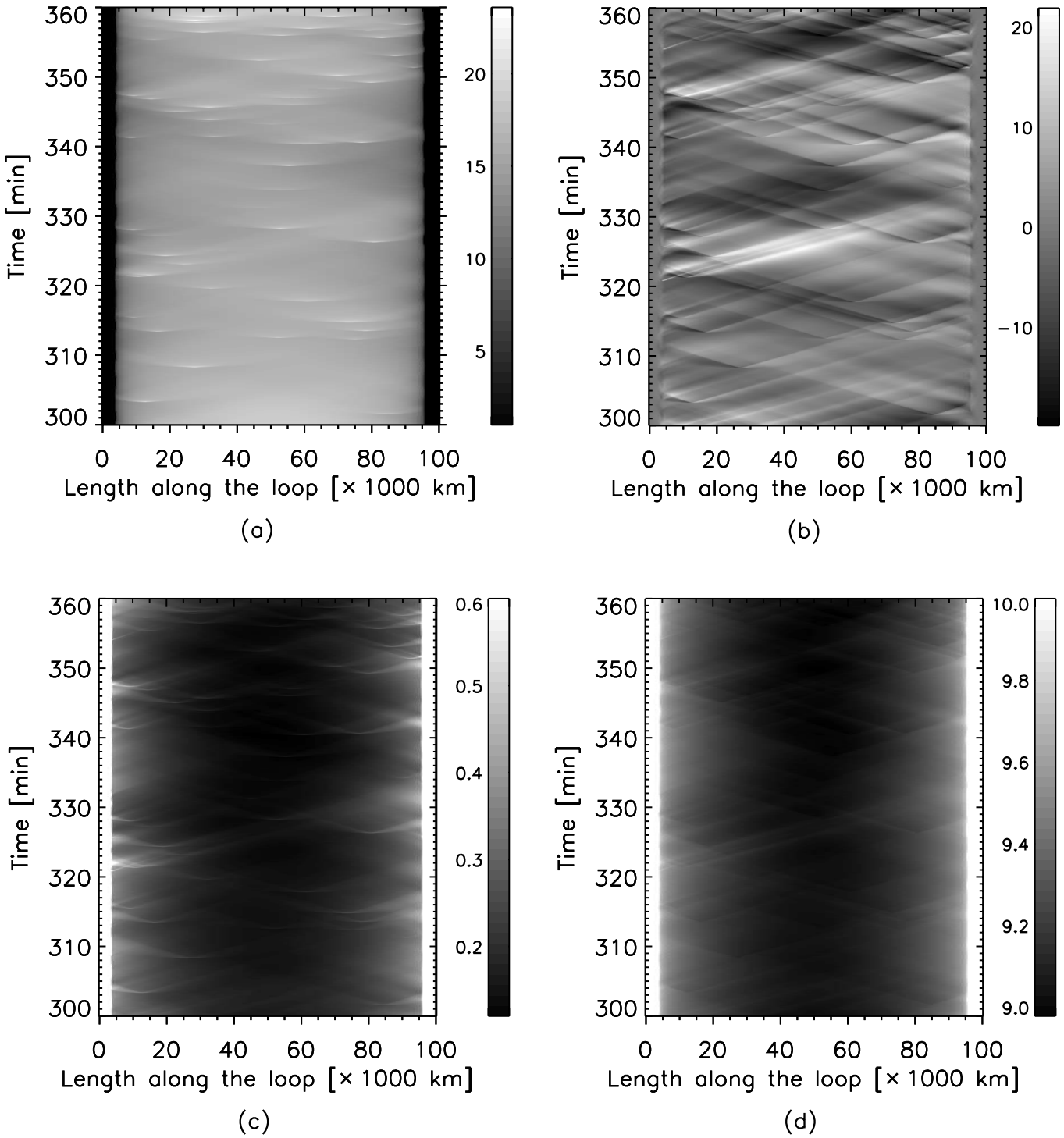

FIG. 6.—Evolution of (*a*) temperature, (*b*) poloidal velocity, (*c*) pressure, and (*d*) density from $t = 300$ to 360 minutes for a loop with heating events uniformly distributed along the loop above a height of 2 Mm. The temperature, pressure, and density maps are saturated above the specified maximum value.

Fig. 5), and a loop with heating events uniformly distributed along the loop (whose energies are uniformly distributed in frequency; same loop as in Fig. 6). In Figure 9 we show intensity histograms constructed from the intensity fluxes of Figure 8. For constructing the histograms we define the intensity of an event as the corresponding intensity peak value in the intensity flux profile minus the previous minimum. A constant logarithmic bin is chosen such that two events with intensities I_1 and I_2 belong to the same bin if they satisfy $\log I_1 - \log I_2 \leq b$, where b denotes the size of the bin. The probability density function corresponding to our events is then

$$\frac{dN(I)}{dI} \simeq \frac{\Delta N(I)}{\Delta I} = \frac{N(I < I^* < I + \Delta I)}{I(10^b - 1)}. \qquad (23)$$

The intensity histograms for all simulation runs are constructed trying different values for the bin, from 0.05 to 0.2. The panels of Figure 9 are distributed in the same way as the panels of Figure 8.

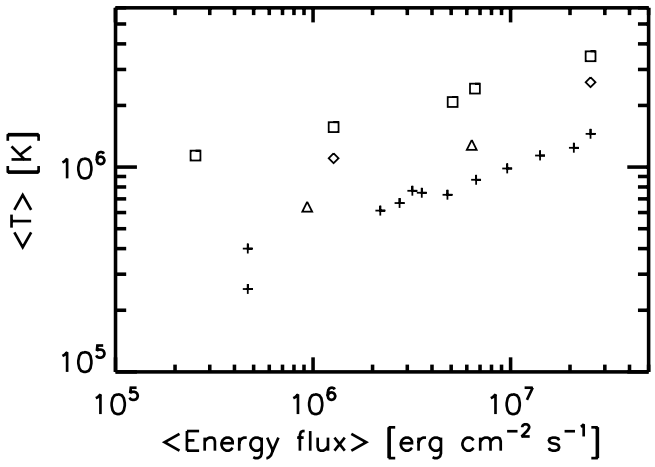

FIG. 7.—Mean temperature in the corona with respect to the mean energy flux input from the heating events simulating nanoflares. Squares designate loops which heating events are randomly (uniformly) distributed along their lengths above a height of 2 Mm from the photosphere. All other symbols designate loops with heating events concentrated toward their footpoints. Diamonds correspond to loops with heating events concentrated in the loop range defined by $\{s_{\min} = 2, s_{\max} = 20\}$ Mm (see eq. [14]). Triangles are for loops with $\{s_{\min} = 2, s_{\max} = 12\}$ Mm, and crosses are for loops with $\{s_{\min} = 1, s_{\max} = 10\}$ Mm.

We can see that all panels display distributions which can be approximated by a power law $dN/dI \propto I^{\delta}$ to a certain extent. In the case of heating concentrated toward the footpoints we obtain broken intensity histograms which can be approximated by two power laws (cf. middle panels of Fig. 9). For this case we concentrate on the high intensity range, corresponding to the range which can actually be observed. All models display power-law ranges that oscillate between 1 and 3 orders of magnitude, where the most robust power-law distributions correspond, as would be expected, to the models having, as an input, energies distributed as a power law. The value of the calculated power-law index in all models is quite robust with respect to the bin size (a variation of less than 0.2 is observed).

4.2. *Discussion*

Figure 8 show that the profile of the intensity flux in the case of the Alfvén wave heated loop is very spiky and remains so when going from the top of the transition region toward the apex. This reflects the highly dynamical state of the corona, which is permeated by strong slow and fast shocks. Correspondingly, the intensity histograms in Figure 9 (*left*) display power-law indexes δ steeper than -2, which remain roughly constant when shifting the observed region along the corona. This is shown by Figure 10 (*left*), in which the power-law index δ is plotted with respect to length along the loop from the transition region to the apex of the loop. The initial increase in value for the power-law index is due to the fact that in the Alfvén wave model the height of the transition region can reach heights above 10 Mm, hence producing, for heights below $\sim$12 Mm, low temperatures for which the thin Al mesh filter of XRT is not sensitive. The constancy of the power-law index in the rest of the loop is due to the uniformly distributed shock heating causing both weak and strong intensity peaks everywhere in the corona. The mean value of the power-law index in this case is $\langle\delta\rangle \sim -2.3$ indicating that most of the heating comes from small energetic events due to the shocks (Hudson 1991). On the other hand, the intensity flux for the case of a loop with nanoflare heating concentrated at the footpoints is less spiky as shown by the middle panels of Figure 8. The farther away we "observe" from the top of the transition region, the less spiky the intensity profile becomes. The middle panels in Figure 9 correspondingly show a power-law index which close to the footpoint has a value of $\delta = -1.86$ ($\simeq\alpha$) and decreases in magnitude to a value $\delta \sim -1.5$ at the apex. The decrease in the power-law index with height can be appreciated in the middle panel of Figure 10. This

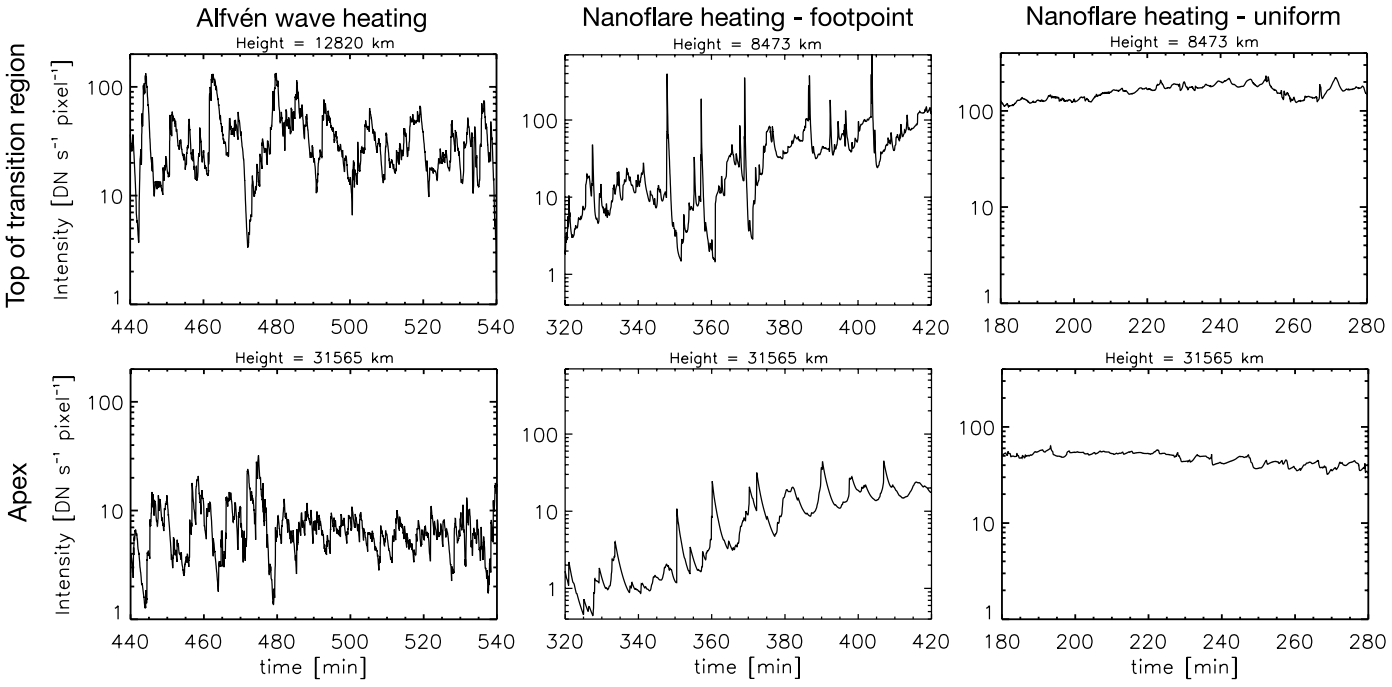

FIG. 8.—Intensity flux time series constructed from *Hinode* XRT response function (Thin Al mesh filter). Top and bottom row panels correspond, respectively, to the top of the transition region and apex of the loop as "observed" regions (the corresponding height is indicated on the top of each panel). From left to right we have, respectively, a loop heated by Alfvén waves, a loop with heating events concentrated toward the footpoints whose energies follow a power-law distribution in frequency with an index of $\alpha = -1.8$, and a loop with heating events uniformly distributed along the loop and whose energies are uniformly distributed in frequency.

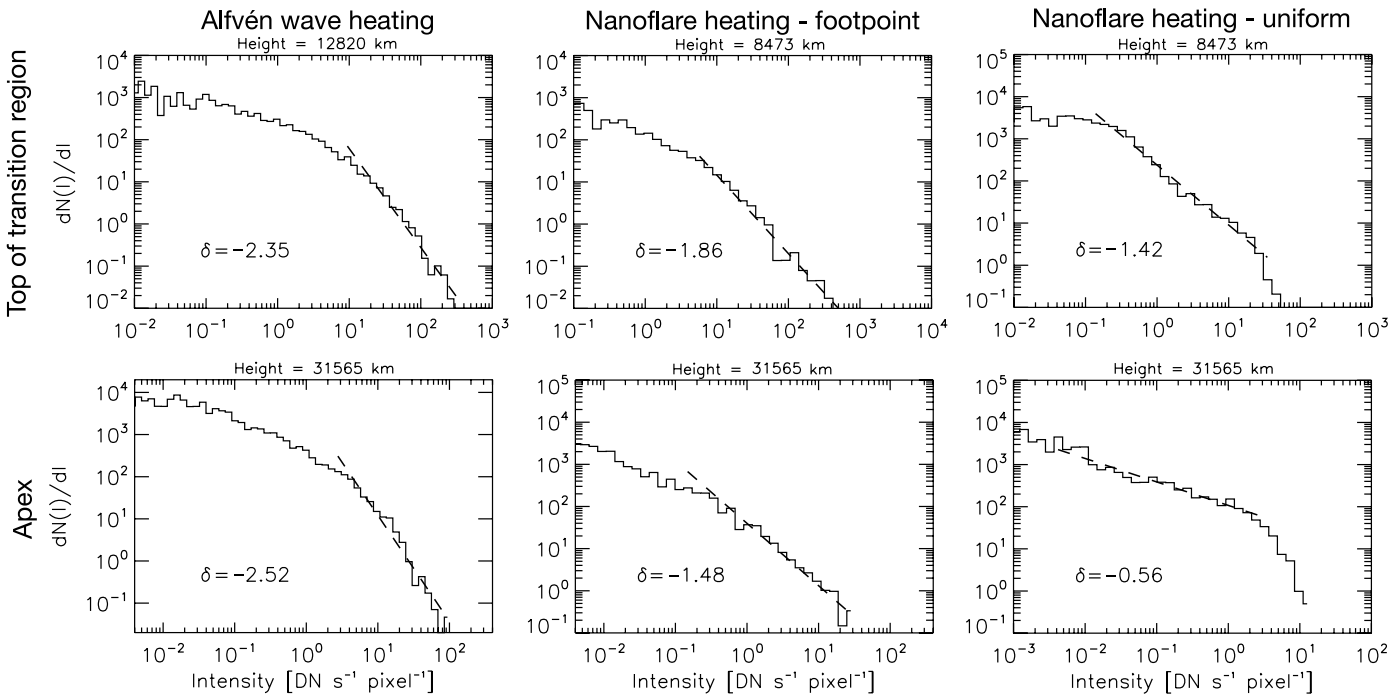

FIG. 9.— Intensity histograms constructed from the intensity flux time series in Fig. 8. Top and bottom panels correspond, respectively, to the top of the transition region and apex of the loop as "observed" regions (the corresponding height is indicated on the top of each panel). From left to right, column panels correspond, respectively, to a loop heated by Alfvén waves, a loop with heating events concentrated at the footpoints whose energies follow a power-law distribution in frequency with an index of $\alpha = -1.8$, and a loop with heating events uniformly distributed along the loop and whose energies are uniformly distributed in frequency.

tendency is due mainly to two reasons. Acoustic shocks dissipate rapidly leaving only weak shocks at the apex of the loop. The second reason is thermal conduction which, in the case of footpoint concentrated heating, is highest at the top of the transition region and damps the small temperature perturbations. Hence, the number of low intensity peaks decreases as the height of the "observed" region increases, whereas the number of high intensity peaks stays roughly constant. As a consequence, the slope of the distribution $dN(I)/dI$ decreases. This effect is more dramatic for uniform nanoflare heating, as shown by the right panels of Figures 8 and 9. In this case maximum temperatures are found at the apex of the loop. Also, mean coronal temperatures are higher than for footpoint concentrated heating. Consequently, thermal conduction flattens intensity peaks much more effectively. As shown by Figure 10 (*right*), the power-law index of the intensity distribution rapidly becomes shallow and stays constant with a value lower than −1 as the "observed' region moves toward the apex, reflecting the low coronal dynamics.

In Moriyasu et al. (2004) a similar figure to Figure 9 was shown where the number of observed heating events was found to follow a power-law distribution with an index of −1.7 using *Yohkoh* SXT and −1.9 using *TRACE* EUV (please refer to Fig. 4 in that paper). The apparent disagreement between these results with the present results can be explained by considering the difference in the used filters. In Moriyasu et al. (2004) the filter Mg of *Yohkoh* SXT is used, which is similar to the thin Be filter of *Hinode* XRT. This filter is less sensitive to lower temperatures than the thin Al mesh filter of XRT, hence the number of small energetic events detected with the thin Be filter is reduced, thus decreasing (in absolute value) the power-law index. Furthermore, the range in intensity which was taken in Moriyasu et al. (2004) extends only over 1 order of magnitude. In Figure 11 we

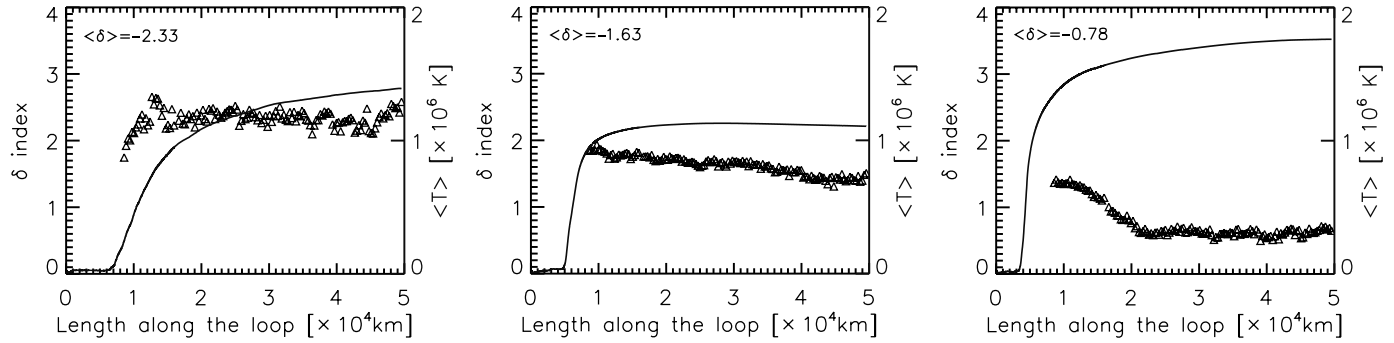

FIG. 10.— Power-law index δ with respect to length along half of the loop for each heating model. The power-law indexes are obtained from the intensity histograms of Fig. 9. The left panel corresponds to the loop heated by Alvén waves, the center panel corresponds to a loop with heating events concentrated toward the footpoints having a power-law spectrum in energies with an index of $\alpha = -1.8$, and the right panel corresponds to a loop with uniformly (randomly) distributed heating events with a uniform spectrum in energies. The solid line (and the corresponding right axis) denotes the mean temperature along the loop (taken over the entire simulation time). The value on the top left corner of each panel denotes the mean value of δ over half the loop.

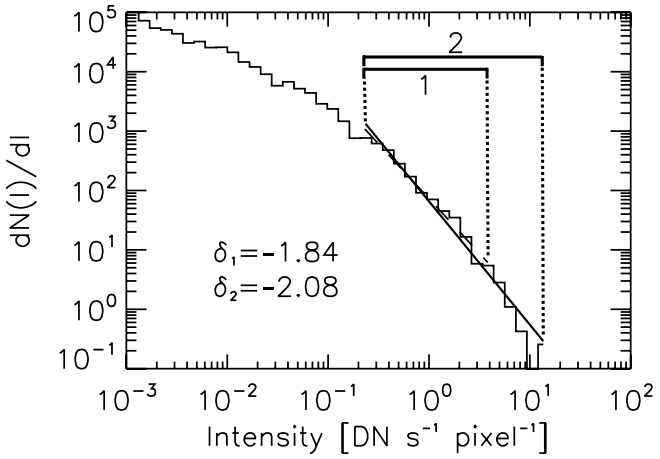

FIG. 11.—Intensity histogram calculated from an intensity flux profile obtained using the filter Thin Be of *Hinode* XRT, which is similar to the filter Mg of *Yohkoh* SXT used in Moriyasu et al. (2004). The dashed line corresponding to range "1" is a power-law fit with index δ_1 using the same range as in Moriyasu et al. (2004). The solid line over the extended range "2" is a power-law fit with index δ_2.

show an intensity histogram calculated from an intensity flux profile of *Hinode* XRT using the filter thin Be. We take a loop with the same characteristics (no subphotospheric region, 20 km of spatial resolution throughout the loop) and an amplitude for the photospheric driver such as to generate the same photospheric velocity amplitude as in their work ($\sim$2.0 km s^{-1}). Making a power-law approximation on the same range as in that work we find an index of -1.84. However, letting the range of the power law account for the highest observed intensities, the index of the distribution becomes steeper than -2 (Fig. 11).

Nanoflare heating concentrated toward the footpoints whose heating events have a power-law spectrum in energies (with a power-law index α) display intensity histograms with a power-law spectrum as well (with a power-law index δ). An interesting and natural question is then whether the power-law indexes of these two distributions are the same or not. Equivalently, we ask whether the "observed" heating events in the loop are the same as the events that are actually taking place in the loop. The answer to this question is given by Figure 10 (*middle*), which corresponds to a loop with heating events concentrated toward the footpoints with a power-law spectrum in energies with an index $\alpha = -1.8$. We can see that $\alpha \simeq \delta$ close to the transition region but as we move toward the apex, δ decreases (in absolute value) toward a value of -1.5 due to the fast dissipation of the slow modes and to the damping by thermal conduction. Information of the small energetic events is lost in the high corona. This implies that the measurement of the power-law index depends on the temperature sensitivity of the used filter, making temperature a strong bias in the determination of this quantity. This could explain the existing discrepancies in measurements of the power-law index when different emission lines are considered (cf. Table 1 in Benz & Krucker 2002; for more studies see, e.g., Aschwanden 2004; Erdélyi & Ballai 2007).

5. CONCLUSIONS

In this work we analyze a way to distinguish observationally between two coronal heating mechanisms: Alfvén wave heating and nanoflare reconnection heating. We have seen that Alfvén wave heated coronae are uniformly heated by strong slow and fast shocks coming from the nonlinear mode conversion of the Alfvén waves into the longitudinal slow and fast modes. The ubiquitous strong shocks can create a thermally stable million degree corona when the photospheric velocity field is above $\sim$1.3 km s^{-1}. The flow structures are complex with many velocity scales lacking uniformity. High-speed flows back and forth from one footpoint to the other are a signature of this heating mechanism. The resulting *Hinode* XRT intensity profiles show spiky patterns from the top of the transition region throughout the corona. As a consequence intensity histograms show a distribution which stays roughly constant in this region, and which can be approximated by a power law with an index steeper than -2, indicating that the main heating comes from small dissipative events.

On the other hand, in the nanoflare heating picture, when heating events are concentrated toward the footpoints coronae show strong slow shocks close to the transition region. Damping by thermal conduction and the fast dissipation of the slow shocks create only weak shocks close to the apex of the loop. Continuous and simultaneous flows from both footpoints are obtained, tending to cross at the apex. Fast speeds are achieved only in the case of footpoint heating. Spiky patterns result in the XRT intensity profiles close to the transition region and a flattening of the profile at the apex. Consequently the intensity histograms show power-law distributions whose indexes decrease the farther we "observe" in the corona from the footpoints of the loop. As information of the small energetic events is lost in the high corona the measured power-law index corresponds to the actual power-law index only close to the transition region. In the case of uniformly distributed heating events the higher coronal temperatures lead to stronger flattening by thermal conduction of the intensity profiles and strong dissipation of the slow shocks. The intensity profiles are not spiky but rather uniform in time. It results in an average power-law index of the distribution in the intensity histogram close to -1. The differences between the coronal heating mechanisms is summarized in Table 3.

TABLE 3
OBSERVATIONAL SIGNATURES FOR CORONAL HEATING MECHANISMS

Heating Model (1)	Flow Pattern (2)	Mean Velocities $\langle v_p \rangle$ (km s^{-1}) (3)	Max Velocities $\langle v_p \rangle$ (km s^{-1}) (4)	Intensity Flux Pattern (5)	Mean Power-Law Index (6)
Alfvén wave	Nonuniform, alternating	$\sim$50	>200	Bursty everywhere	$\langle \delta \rangle < -2$
Nanoflare footpoint	Uniform, simultaneous	$\sim$15	>200	Bursty close to TR	$-1.5 > \langle \delta \rangle > -2$
Nanoflare uniform	Uniform, simultaneous	$\sim$5	<40	Flat everywhere	$\langle \delta \rangle \sim -1$

NOTES.—Col. (1): Heating model, Alfvén wave heating, nanoflare reconnection heating with the heating events concentrated toward the footpoints ("Nanoflare footpoint") or uniformly distributed along the loop ("Nanoflare uniform"). Col. (2): The pattern of the flows along the loop obtained with each heating model. "Alternating" and "simultaneous" correspond, respectively, to flows from one footpoint to the other that alternate in time or are rather simultaneous (zigzag shape or X shape, respectively, in Figs. 3*b*, 5*b*, and 6*b*). Flows are "uniform" when their paths can be traced easily along the loop (cf. § 3.3). Cols. (3) and (4): The mean and maximum flow velocities (in km s^{-1}) found in each heating model, respectively. Col. (5): The intensity flux pattern, which refers to the shape of the intensity flux time series, which can be bursty or rather flat, and which can change with position along the loop (cf. § 4.2). Col. (6): The mean power-law index, which denotes the mean over the power-law indexes obtained from the intensity histograms for many positions along the loop from the transition region to the apex.

The power-law index of the heating distribution is thus found to be sensible to the location of the heating along the loop. Furthermore, Alfvén wave heating and nanoflare heating are found to exhibit different power-law indexes. This quantity thus not only has information about the role of small heating events toward the overall heating but also about the location of the heating along the loop and about the operating heating mechanism. It is thus a powerful tool that can shed some light into the coronal heating problem.

P. A. would like to thank T. Suzuki, H. Isobe, L. Heggland, T. Magara, R. Erdélyi, M. Carlsson, and V. Hansteen for many fruitful discussions. P. A. would also like to acknowledge J. Candamil for patient encouragement. This work was supported by the Grant-in-Aid for the Global COE Program "The Next Generation of Physics, Span from Universality and Emergence" from the Ministry of Education, Culture, Sports, Science and Technology (MEXT) of Japan, by a Grant from the International Astronomical Union, and by a Grant-in-Aid for Creative Scientific Research, "The Basic Study of Space Weather Prediction" (17GS0208; Head Investigator: K. Shibata), from the Ministry of Education, Science, Sports, Technology, and Culture of Japan. The numerical calculations were carried out on Altix3700 BX2 at YITP in Kyoto University. The authors thank the anonymous referee for constructive remarks.

REFERENCES

Anderson, C. S., & Athay, R. G. 1989, ApJ, 336, 1089
Antiochos, S. K., MacNeice, P. J., Spicer, D. S., & Klimchuk, J. A. 1999, ApJ, 512, 985
Aschwanden, M. J. 2001, ApJ, 559, L171
———. 2004, Physics of the Solar Corona: An Introduction (Springer: Berlin)
Aschwanden, M. J., Schrijver, C. J., & Alexander, D. 2001, ApJ, 550, 1036
Alfvén, H. 1947, MNRAS, 107, 211
Benz, A. O., & Krucker, S. 2002, ApJ, 568, 413
Cargill, P. J., & Klimchuk, J. A. 2004, ApJ, 605, 911
Erdélyi, R. 2004, Astron. Geophys., 45, 34
Erdélyi, R., & Ballai, I. 2007, Astron. Nachr., 328, 726
Evans, C. R., & Hawley, J. F. 1988, ApJ, 332, 659
Golub, L., et al. 2007, Sol. Phys., 243, 63
Hollweg, J. V., Jackson, S., & Galloway, D. 1982, Sol. Phys., 75, 35
Hori, K., Yokoyama, T., Kosugi, T., & Shibata, K. 1997, ApJ, 489, 426
Hudson, H. S. 1991, Sol. Phys., 133, 357
James, S. P., & Erdélyi, R. 2002, A&A, 393, L11
Katsukawa, Y., & Tsuneta, S. 2001, ApJ, 557, 343
Krucker, S., & Benz, A. O. 1998, ApJ, 501, L213
Kudoh, T., Matsumoto, R., & Shibata, K. 1998, ApJ, 508, 186
Kudoh, T., & Shibata, K. 1999, ApJ, 514, 493
Landini, M., & Monsignori Fossi, B. C. 1990, A&AS, 82, 229
Mendoza-Briceño, C. A., & Erdélyi, R. 2006, ApJ, 648, 722
Mendoza-Briceño, C. A., Erdélyi, R., & Sigalotti, L. Di G. 2002, ApJ, 579, L49
Mendoza-Briceño, C. A., Sigalotti, L. Di G., & Erdélyi, R. 2005, ApJ, 624, 1080
Moriyasu, S., Kudoh, T., Yokoyama, T., & Shibata, K. 2004, ApJ, 601, L107
Moriyasu, S., & Shibata, K. 2004, Coronal Heating, ed. R. W. Walsh (ESA SP-575; Noordwijk: ESA), 80
Müller, D. A. N., Hansteen, V. H., & Peter, H. 2003, A&A, 411, 605
Musielak, Z. E., Routh, S., & Hammer, R. 2007, ApJ, 659, 650
Noble, M. W., Musielak, Z. E., & Ulmschneider, P. 2003, A&A, 409, 1085
Parker, E. N. 1988, ApJ, 330, 474
———. 1991, ApJ, 372, 719
Parnell, C. E., & Jupp, P. E. 2000, ApJ, 529, 554
Patsourakos, S., & Klimchuk, J. A. 2005, ApJ, 628, 1023
Patsourakos, S., & Vial, J.-C. 2002, A&A, 385, 1073
Priest, E. R., Foley, C. R., Heyvaerts, J., Arber, T. D., Culhane, J. L., & Acton, L. W. 1998, Nature, 393, 545
Rosner, R., Tucker, W. H., & Vaiana, G. S. 1978, ApJ, 220, 643
Shibata, K., Tajima, T., Matsumoto, R., Horiuchi, T., Hanawa, T., Rosner, R., & Uchida, Y. 1989a, ApJ, 338, 471
Shibata, K., Tajima, T., Steinolfson, R. S., & Matsumoto, R. 1989b, ApJ, 345, 584
Shimizu, T. 1995, PASJ, 47, 251
Spadoro, D., Lanza, A. F., Karpen, J. T., & Antiochos, S. K. 2006, ApJ, 642, 579
Spadoro, D., Lanza, A. F., Lanzafame, A. C., Karpen, J. T., Antiochos, S. K., Klimchuk, J. A., & MacNeice, P. J. 2003, ApJ, 582, 486
Stone, J. M., & Norman, M. L. 1992, ApJS, 80, 791
Takeuchi, A., & Shibata, K. 2001, ApJ, 546, L73
Taroyan, Y., Bradshaw, S. J., & Doyle, J. G. 2006, A&A, 446, 315
Taroyan, Y., Erdélyi, R., Doyle, J. G., & Bradshaw, S. J. 2007, A&A, 462, 331
Uchida, Y., & Kaburaki, O. 1974, Sol. Phys., 35, 451
Walsh, R. W., Bell, G. E., & Hood, A. W. 1997, Sol. Phys., 171, 81
Wentzel, D. G. 1974, Sol. Phys., 39, 129
Yabe, T., & Aoki, T. 1991, Comp. Phys. Comm., 66, 219
Yokoyama, T. 1998, Solar Jets and Coronal Plumes, ed. T. D. Guyenne (ESA SP-421; Noordwijk: ESA), 215